Review 2

Crystal structure refinement and elasticity of the hexagonal $Na_{0.41}[Na_{0.125}Mg_{0.79}Al_{0.085}]_2[Al_{0.79}Si_{0.21}]_6O_{12}$ (NAL phase)

MARTHA G. PAMATO [1*], ALEXANDER KURNOSOV [1], TIZIANA BOFFA BALLARAN[1], DMYTRO M. TROTS [1], RAZVAN CARACAS [2] AND DANIEL J. FROST [1]

[1] Bayerisches Geoinstitut, Universitaet Bayreuth, D - 95440 Bayreuth, Germany

[2] Laboratoire de Sciences de la Terre, Centre National de la Recherche Scientifique, Ecole Normale Supérieure de Lyon, 46 allée d'Italie, 69364 Lyon Cedex 07, France

[*] martha.pamato@uni-bayreuth.de

ABSTRACT

At lower mantle conditions, subducted mid oceanic ridge basalts (MORB) will crystallize more than 20 vol. % of an aluminium rich phase, which is referred to generally as the NAL (new aluminium) phase. Given that a significant proportion of the lower mantle may be comprised of subducted crust, the NAL phase may contribute to the bulk elastic properties of the lower mantle. In this study we report for the first time the structure, Raman spectrum and elasticity of single-crystals of $Na_{0.41}[Na_{0.125}Mg_{0.79}Al_{0.085}]_2[Al_{0.79}Si_{0.21}]_6O_{12}$ NAL phase, synthesized at 2260 °C and 20 GPa. The single-crystal structure refinement of NAL, which is consistent with the space group $P6_3/m$, reveals dynamic disorder of Na atoms along channels within the structure. The elastic tensor was experimentally determined at ambient conditions by Brillouin scattering spectroscopy. The elastic modulii obtained from the Voigt-Reuss-Hill approximation using the elastic constants determined in this study are K_S = 206 GPa and μ = 129 GPa, whereas the isotropic compressional and shear sound velocities are V_P = 9.9 km/s and V_S = 5.8 km/s. The NAL phase is elastically anisotropic, displaying 13.9 % compressional and shear wave anisotropy. Elastic constants as well as Raman active modes of NAL have also been calculated using density-functional theory and density-functional perturbation theory.

Keywords: NAL phase, Brillouin spectroscopy, Single-crystal X-ray diffraction, lower mantle, elasticity.

INTRODUCTION

As a consequence of plate tectonics, basaltic oceanic crust is subducted into the mantle. The subduction of oceanic lithosphere plays an important role in the dynamics of mantle convection and is believed to be responsible for the creation of lateral chemical heterogeneity in the mantle (Helffrich and Wood 2001). In this context, the high pressure and temperature metamorphic phases which recrystallize from basic rocks that form the oceanic crust are likely to be important components of the lower mantle and as such to influence its physical and chemical properties. Several high pressure studies on MORB bulk composition have shown that various Al rich phases can form under lower mantle conditions (Irifune and Ringwood 1993; Kesson et al. 1994; Irifune et al. 1996; Akaogi et al. 1999; Miyajima et al. 1999, 2001). In particular, Irifune and Ringwood (1993) first reported the breakdown of majorite garnet to an assemblage of Mg-Perovskite, Ca-Perovskite and a separate aluminous phase at pressure and temperature conditions of the lower mantle. This so called new Al phase or NAL has a hexagonal crystal structure and can contain several different cations, such as Na, K, Ca, Mg and Fe (Akaogi et al. 1999; Miura et al. 2000; Gasparik et al. 2000; Miyajima et al. 1999, 2001). NAL is therefore likely to be the main host for alkali elements in oceanic crust that has been subducted to ~ 600-1300 km (Miyajima et al. 2001). Due to the extremely long time scale required for the chemical equilibration of subducted crustal heterogeneities in the lower mantle (Holzapfel et al. 2005), it has also been proposed that the bulk of the mantle might be a mechanical mixture between a depleted mantle residue and subducted crustal components (Xu et al. 2008). In this case NAL is likely to form a major part of the crustal component.

Recently, Walter et al. (2011) described sublithospheric diamonds hosting composite multiphase inclusions with compositions encompassing phase assemblages expected to crystallize from basic

crustal material under lower-mantle conditions. In particular, Walter et al. (2011) suggested that some of these inclusions were present as the NAL phase at lower mantle conditions, giving further support for the existence of this phase in the Earth's lower mantle. The elastic properties of NAL, hence, may influence the bulk elastic properties of the lower mantle.

NAL phases crystallising in MORB compositions display complex solid solutions and have the general formula $XY_2Z_6O_{12}$ where X represent a large monovalent or divalent cation (Ca^{2+}, K^+, Na^+), Y a middle-sized cation (Mg^{2+}, Fe^{2+} or Fe^{3+}), and Z a small cation (Al^{3+} and Si^{4+}).

To date several studies have been conducted on the structure, stability and compression of NAL phases both in complex and simplified systems (Gasparik et al. 2000; Miura et al. 2000; Kojitani et al. 2011; Imada et al. 2011, 2012; Kawai and Tsuchiya, 2012). However, only in one study (Gasparik et al. 2000), a single-crystal structural analysis has been reported on NAL with the formula $[K_{0.56}Na_{0.32}][Ca_{0.04}Mg_{1.66}Fe^{2+}_{0.3}][Mg_{0.98}Fe^{3+}_{0.3}Al_{2.62}Si_{2.1}]O_{12}$. All other studies (Miura et al. 2000; Kojitani et al. 2011) dealt with powdered samples. The crystal structure of NAL consists of a double chain of $M1O_6$ octahedra connected by shared edges, occupied by the Z cations. The M2 site is a six fold coordinated triangular prism occupied by the Y cations and surrounded by three double chains of $M1O_6$ octahedra. The larger channels (M3 site) are formed by six double chains of $M1O_6$ octahedra and are occupied by the large X cations.

Single-crystals of $Na_{0.41}[Na_{0.125}Mg_{0.79}Al_{0.085}]_2[Al_{0.79}\ Si_{0.21}]_6O_{12}$ NAL have been synthesized for this study at lower mantle conditions with a composition close to that expected to crystallise in a subducting slab. We report, for the first time, an experimental determination of the full elastic tensor of this NAL by Brillouin scattering spectroscopy as well as a structural refinement and Raman spectrum. We complement the experimental observations with first-principles calculations, performed using density-functional theory and density-functional perturbation theory.

EXPERIMENTAL METHODS

Sample synthesis and characterization

For the synthesis of the new aluminium phase, a starting composition was prepared by mixing oxides and carbonates in stoichiometric proportions, to give the following composition after decarbonation: 10.9% Na_2O (starting from Na_2CO_3), 14.2% MgO, 21.1% SiO_2, 53.8% Al_2O_3 (expressed in wt %). The reagents were first dried, then weighed and mixed. In order to decarbonate the sodium carbonate, the mixture was placed in a platinum (Pt) crucible, heated up to 1000 °C in 10 hours and kept at this temperature for 6-7 hours.

The decarbonated powdered sample was loaded into a capsule fabricated from a 1 mm diameter rhenium rod spark eroded with a hole of approximately 0.5 mm deep and 0.5 mm in diameter. The capsule was closed by placing a rhenium foil on top of the rod. For the synthesis of high quality single-crystals of NAL it was necessary to perform experiments slightly above the dry melting solidus at temperatures in excess of 2200 °C and pressures of 20 GPa. This high melting temperature demonstrates a remarkable change in the melting behaviour of Na-rich phases compared to lower pressures.

High-pressure syntheses were carried out using a 1200 tonne multi-anvil apparatus at the Bayerisches Geoinstitut (BGI). A 10 mm edge length Cr_2O_3-doped MgO octahedron was employed as a pressure medium with tungsten carbide cubes of 32 mm edge length and truncations of 4 mm edge length (10/4 assembly). The temperature was measured using W3%Re / W25%Re (type D) thermocouple wires (0.13 mm thick) that were inserted axially into the octahedral assembly, with the hot junction in contact with the capsule.

Details of the pressure calibrations for the assembly used in this study are reported in Keppler and Frost (2005). The sample was first pressurized up to 20 GPa and heated up to 1500 °C over 15 minutes. The temperature was kept at 1500 °C for 15 minutes and then finally heated rapidly to 2260 °C in 3 minutes. After heating at high pressure for 5 minutes, the experiment was quenched isobarically by shutting off the power and the sample was recovered after slow decompression over 18 hours.

Recovered samples were mounted in epoxy and polished. Single-crystals of the NAL phase (up to 120 μm in length) were found coexisting with quenched melt in the mounted sample (Figure1). The element concentrations were measured with a JEOL JXA-8200 electron microprobe (EMPA), operating at 15 kV and 5 nA. Diopside, spinel, forsterite and albite were used as standards for determining the concentrations of Si, Al, Mg and Na respectively. The analyses indicated the following composition of the NAL phase (run number S5253) in weight %: 7.8 (2)% Na_2O, 14.9 (3)% MgO, 17.7 (4)% SiO_2, 58.8 (4)% Al_2O_3, which recalculates to the chemical formula $Na_{1.07}Mg_{1.58}Al_{4.91}Si_{1.26}O_{12}$.

Raman spectroscopy was performed on the same NAL single-crystal (s5253x5) used for the elasticity study employing a Dilor XY system operating with a 514 nm Ar^+ ion laser equipped with a liquid nitrogen-cooled CCD detector.

Single-crystal data collection and structure refinements

A NAL single-crystal (s5253x5) of a suitable size (70x50x15μm) and optically free of defects was selected from the capsule and mounted on a glass fiber for single crystal diffraction. Data collection was performed on an Xcalibur diffractometer (operated at 50 kV and 40 mA and equipped with a CCD detector) using Mo*K*α radiation (graphite monochromator). Several ω scans were chosen to obtain coverage of the full reciprocal sphere up to $2\theta_{max} = 70°$, with an exposure time of 80 s/frame and a crystal detector distance of 45 mm. Lorentz and polarization factors together with an analytical absorption correction based on the crystal shape were employed for the correction of the reflection intensities using the CrysAlis package (Oxford Diffraction 2006).

The measured reflections were consistent with the hexagonal space group $P6_3/m$ and resulted in a total of 328 unique reflections with a discrepancy factor $R_{int} = 0.031$. Structure refinements were performed based on F^2 using the SHELX97 program package (Sheldrick 2008) in the WingX System (Farrugia 1999) starting from the atomic structural parameters reported by Kojitani et al. (2011). Atomic scattering factors for Si, Al, Mg, Na and O were used and all atoms were refined

anisotropically. The resulting discrepancy factor after convergence of the refinement cycles, however, resulted in a quite large value, i.e. R1 = 0.135 for the 308 observable reflections [$F_o > 4\sigma(F_o)$]. A test for possible merohedral twinning of the crystal gave a positive result, with the following twin law: $R = \begin{pmatrix} 0 & 1 & 0 \\ 1 & 0 & 0 \\ 0 & 0 & -1 \end{pmatrix}$. Where R is the matrix that transforms the *hkl* indices of one component into the other. By introducing such a transformation into the refinement process the discrepancy factor decreases to R1 = 0.028 and the resulting proportions of the two twin components were refined as 75 % and 25 %, respectively. In the last refinement cycles the chemistry of the crystal obtained from the microprobe analysis was taken into account, therefore the site occupancies of the different sites were fixed as follows: 0.79 Al + 0.21 Si for M1; 0.085 Al + 0.79 Mg + 0.125 Na for M2 and the remaining Na was inserted into M3, which has therefore an occupancy of only 0.41. The anisotropic displacement parameter indicates that the thermal ellipsoid of Na at the M3 site is elongated along the *c* axis. A refinement that included a split-site model with isotropic displacement parameters was also tested, but this resulted in no improvement of the discrepancy factor and gave a negative displacement parameter for one of the split sites. Therefore, the split-site model was abandoned. Details of the data collection and structural refinements, atomic positions and displacement parameters, as well as selected bond distances and angles are reported in Tables 1, 2 and 3, respectively.

Simultaneous X-ray diffraction and Brillouin scattering

Both the single-crystal used for the X-ray data collection and structure refinements (s5253x5) and another high quality single-crystal (70x70 μm) made in the same experiment (s5352x3) were selected for Brillouin scattering measurements and were polished into parallel plates with a thickness of approximately 15 μm. The crystals were then loaded into two piston cylinder diamond

anvil cells (Kantor et al. 2012) for X-ray and Brillouin measurements (see inset of Figure 1). No pressure medium was employed in the cells as the measurements were performed at room pressure. Simultaneous acquisition of density and sound velocities of the NAL crystals was performed at the Bayerisches Geoinstitut. X-ray measurements were performed with a rotating anode X-ray source (FR-E^+ SuperBright from Rigaku with MoKα radiation) equipped with multilayer VaryMax^{TM} focusing optics. A detailed description of this system can be found in Trots et al. (2011). The lattice parameters were determined using the eight-position centering of 10-16 Bragg reflections ($20<2\theta<29$ degrees) according to the procedure of King and Finger (1979). The resulting unit cell volumes are 182.00 (5) $Å^3$ and 181.92 (7) $Å^3$ for s5253x3 and s5253x5, respectively, in agreement with the value obtained for sample s5253x5, 182.3 (2) which has a lower accuracy due to the use of an area detector. Typical half-widths of the reflections were between 0.080 and 0.090° in ω profiles. Brillouin scattering measurements were performed with a six-pass Sandercock-type tandem Fabry-Pérot interferometer using a coherent Verdi V2 solid state Nd:YVO_4 frequency doubled laser (λ = 532.0 nm) as a light source. The measured sample plates have normal vectors of (0.04397, -0.07541, 0.0997) and (0.05505, 0.11433, -0.03807) and starting phonon directions of (0.33506, 0.12554, -0.05278) and (0.32600, -0.15670, 0.00125). All spectra were collected in 80° forward symmetric/platelet scattering geometry, so that knowledge of the refractive index of the sample, diamond anvils and pressure medium is not required (Whitfield et al. 1976; Sinogeikin and Bass 2000). Brillouin spectra of the NAL crystals were collected with a laser power of 150 mW. Typical collection times for each crystal orientation were 4 hours. In total, 14 crystallographic directions were sampled, 4 for crystal s5253x3 and 10 for crystal s5253x5. Sound velocities were determined from the frequency shifts using the following relationship (Whitfield et al. 1976): $V = \Delta\nu*\lambda_0/2*\sin(\theta/2)$, where ν is the measured Brillouin shift, λ_0 is the incident laser wavelength, θ is the external scattering angle. Dispersion curves of sound velocities versus crystallographic orientation were collected by changing the crystal orientation through movement of the χ–circle of the Eulerian cradle. The phonon direction (obtained from the UB orientation matrix determined

from the diffraction experiments) was related to the orientation at any χ via a general Cartesian rotation matrix. The experimental sound velocities, obtained from the previous equation, are a function of the crystallographic orientation q, the single crystal elastic moduli C_{ij} and the density, and are related through the Christoffel equation: $\left|C_{ijkl}\, q_j q_l - \rho V^2 \delta_{ik}\right| = 0$, where δ_{ik} is the Kronecker delta. This equation is cubic in V^2, i.e., its solutions result in three acoustic velocities $V_{P,S1,S2} = f(\rho, C_{ij}, q)$ with quasi-compressional wave (for arbitrary crystallographic orientation) velocity V_P and slow and fast quasi-shear wave velocities V_{S1} and V_{S2}. It is therefore possible to determine both crystal orientation and elastic constants by fitting solutions of the equation of motion to measured sound velocities. In our case, however, crystallographic orientation and density were obtained very precisely through single crystal X-ray diffraction measurements and were therefore fixed. The form of the solutions $V_{P,S1,S2} = f(\rho, C_{ij}, q)$ depend strictly on crystal symmetry and were derived for elastically anisotropic solids as a function of point group symmetry by Every (1980). NAL crystallizes in the hexagonal space group $P6_3/m$ with point group $6/m$ and the corresponding solution of Every (1980) was employed.

The elastic constants C_{ij} were extracted by simultaneously fitting 6 dispersion curves (3 solutions for each crystal) to the experimentally measured acoustic velocities $V_{P,S1,S2} = f(C_{ij})$, using the quasi-Newton minimization of the sum of all residuals squared. The C_{ij} values obtained from ab initio calculations in this study were used as starting values for the minimization process.

First-principles calculations

In parallel with the experiments we performed first-principles calculations based on density-functional theory (Kohn and Sham 1965; Payne et al. 1992; Martin 2003) in the ABINIT implementation, with planewaves and pseudopotentials (Gonze et al. 2002, 2009). First we obtained the crystal structure for the $Na_{1.3}Mg_{1.6}Al_{4.9}Si_{1.2}O_{12}$ composition. While in the experimental structure the Na atoms occupy the 2*d* position of the $P6_3/m$ space group, with 0.41 occupancy, in the ab initio

206 structure, in order to avoid dealing with supercells and disordered structures we ordered the Na
207 atoms on one of the two sites inside the channels, breaking the inversion centre thus lowering the
208 symmetry to *P*-6. Moreover, we considered ideal solid solutions of Na – Al and Al – Si on the 2*d*
209 and 6*h* crystallographic sites, respectively, which were treated using alchemical pseudopotentials
210 (Cohen 2007; Caracas and Banigan 2009). We used a 4x4x8 grid of regular k points (Monkhorst
211 and Pack 1976) 40 Ha (1Ha = 27.2116 eV) kinetic energy cut-off and the standard local-density
212 approximation for the exchange-correlation energy. We then computed the elastic constant tensors,
213 the vibrational modes and Raman spectrum, with both peak positions and intensity, in the
214 framework of the density-functional perturbation theory (Baroni et al. 2001; Gonze et al. 2005;
215 Hamann et al. 2005; Veithen et al. 2005; Caracas and Gonze 2010).
216
217 ## RESULTS AND DISCUSSION
218
219 *Structural model from single-crystal X-ray diffraction*
220 Details of the atomic positions and displacement parameters are reported in Table 2. Selected
221 interatomic distances and angles of the NAL phase are reported in Table 3 and are compared to
222 powder diffraction data from Kojitani et al. (2011). The size of the (Al,Si)O_6 site of NAL in this
223 study is comparable to that of the Na-Hex phase reported by Kojitani et al. (2011), as well as the
224 average M1-O distances and M3-O distances. The M2-O distance of 2.098 (1) Å determined in this
225 study is smaller than that in Na-Hex phase of 2.128 (3), but it is similar to that of K-Hex and Ca-
226 Hex phases reported in the same study and in Miura et al. (2000), respectively. This suggests that
227 the size of the trigonal prism sites does not depend on the presence of Na as previously reported by
228 Kojitani et al. (2011), since in our sample the amount of Na in M2 is larger than that reported for
229 their sample.
230 The most striking feature of the structural refinement reported in this study is the very large Na
231 displacement parameter at the M3 site, which is elongated along the *c* axis, suggesting dynamic

disorder of the Na atoms in the channels along this direction (Figure 2). Gasparik et al. (2000) also observed a pronounced distribution of electron density in the M3 site along the channels. Thus, they reported a model with the M3 site refined at a general position (0, 0, z) instead of the ideal site at (0, 0, ¼). However, since they used an isotropic displacement parameter, they did not observe the large elongation along the *c* axis as in our case.

It is difficult to speculate on the type of dynamic disorder that the Na atoms may have at the conditions of the lower mantle. The effects of increasing *P* and *T* are likely to act in opposite directions. With increasing pressure we might expect freezing of the Na atom motion in one of the two *2d* positions of the channels and a consequent phase transition to a lower symmetry, whereas higher temperatures will favour greater motion and possibly free movement of Na within the NAL M3 channels. Room temperature high pressure studies (Vanpeteghem et al. 2003; Guignot and Andrault 2004; Shinmei et al. 2005; Sanehira et al. 2006; Imada et al. 2012) have not revealed any phase transformation, suggesting that such dynamic disorder may be present also at pressures of the lower mantle. Note, however, that these previous studies have all used powder diffraction information and, therefore, may not have the accuracy required to observe subtle changes driven by ordering of Na in the channels.

Atomic vibrations

The experimental and theoretical Raman spectra of NAL are reported in Figure 3. The complete description of all theoretical Raman modes, containing the relative intensity, the symmetry labels, the description of the atomic vibrations and the proposed correspondence to the experimental modes are given in Table 4. The full description of the theoretical vibrational modes in the zone-center for the NAL phase at experimental density is reported on the WURM website (http://wurm.info; Caracas and Bobocioiu, 2011).

Experimentally, the spectrum consists of broad bands centred at approximately 273, 370, 507, 553, 735, 757 and 1091 cm^{-1}. These broad features are likely due to the Al/Si and Mg/Al/Na disorder in

the M1 site and M2 site, respectively. These broad bands clearly consist of several Raman active modes having very close frequencies as shown by the theoretical calculations. The only major discrepancy between the experimental spectrum and the theoretical calculations is the broad experimental peak around 1000-1200 cm^{-1} that very likely is an overtone of the 553 cm^{-1} band and/or a combination mode of several bands from lower frequency. The differences in peak position between experiment and calculations can be due to both the slightly different chemistry and disorder of the cations among the sites and the different temperature (experiments are at room temperature, whereas calculations are static, i.e. at 0 K). In particular, as stated above, the ordering of Na on one position in the theoretical structure lowers the symmetry and breaks the inversion centre. This results into a different number of Raman-active modes between experiment and calculations, as some of the E_u modes of $P6_3/m$ become Raman-active in P-6. But the peak width and the structural disorder make it hard to distinguish individual peaks in the experiment. With these considerations in mind, we can interpret all major Raman peaks in NAL in terms of the atomic displacement pattern derived from calculations, given the similarity between the calculated and observed spectra. The modes corresponding to the vibration of the Na cations inside the channels lay at the lowermost frequencies, below the experimentally observable range. The Na displacement parallel to the channel axis is an unstable theoretical mode at static conditions (T = 0 K), where the Na atoms are frozen. At high temperatures this instability can be correlated to the observed dynamic disorder of Na along the channels. The in-plane Na displacements within the hexagonal basal plane are found at 148 cm^{-1} in the calculations. The sublattice of octahedra forming the channel walls also participate in this vibration. The other vibrations up to 307 cm^{-1} are various lattice modes, dominated by rigid displacements of the $(Si,Al)O_6$ octahedra or $(Mg,Al)O_6$ polyhedra. The broad features at higher frequency represent different types of asymmetric stretching and bending modes of (Si,Al)-O and (Mg,Al)-O bonds.

Both the experimental Raman spectrum and the full description of the theoretical Raman modes could be used to identify possible NAL phases present in inclusions in diamonds or in meteoritic veins.

Elasticity

A typical Brillouin spectrum of the NAL phase is shown in Figure 4. The collected Brillouin spectra were of excellent quality with a high signal-to-noise ratio and with V_P and the two V_S displaying sharp peaks. The measured acoustic velocities in different crystallographic orientations as a function of χ angle for both crystals at room pressure are shown in Figure 5.

The elastic constants and aggregate properties are listed in Table 5. Our structural refinement model revealed the presence of merohedral twinning. By multiplying the twin law transformation matrix to the orientation matrix of the crystal it was possible to obtain the crystallographic orientation of the twin component. The calculated acoustic velocities as a function of crystallographic angle for the twin component according to the twin matrix are exactly the same as those collected, indicating that this type of twinning does not modify the measured elastic properties of the sample. An analysis of the correlations between the elastic constants, which takes into account the covariance matrix, was performed. The correlation between the constants is small, with a maximum value of 0.814 between C_{11} and C_{12} constants. Aggregate velocities as well as elastic moduli were calculated from the C_{ij}'s using the Voigt-Reuss-Hill averaging scheme (Hill 1952). Uncertainties in the elastic constants were calculated from the covariance matrix but these were supplemented by considering other sources of error inherent to diamond anvil cell measurements (see Sinogeikin and Bass 2000). In this study typical errors are less than 2% in elastic moduli and less than 1% in sound velocities. We obtained K_S = 206 (2) GPa and μ = 129 (1) GPa for the aggregate elastic moduli and V_P = 9.9 and V_S = 5.8 km/s for the isotropic compressional and shear sound velocities. These values, as well as the experimental C_{ij} appear to lie in between the values obtained from theoretical calculations in this study and those previously reported by Kawai and Tsuchiya (2012) (Table 5 and Figure 5). This

discrepancy between experimental and theoretical values is very likely due to the fact that in the synthetic samples the cations are randomly distributed among the crystallographic sites, whereas theoretical calculations have to deal either with ordered structures (as in the case of this study where Na has been allocated only in one of the *2d* positions breaking the symmetry) or with super-cells which preserve the symmetry but have prescribed local ordered configurations (Kawai and Tsuchiya 2012). Note also that our shear velocity and shear modulus are higher than those reported by Dai et al. (2013) for a polycrystalline $Na_{0.4}Mg_{0.6}Al_{1.6}Si_{0.4}O_4$ NAL phase determined by means of Brillouin scattering on a powdered sample (Table 5) likely due to the highly anisotropic behavior of the NAL phase. Using the single-crystal elastic constants and density obtained in this study we can define the room pressure seismic anisotropy ($A= 200 \times [(V_{imax} - V_{imin}) / (V_{imax} + V_{imin})]$) by analyzing a hemisphere of all possible propagation directions (Figure 6). The NAL phase displays 13.9 % shear wave anisotropy (AV_S) which is mainly due to the high anisotropic feature of V_{S2} (14 % anisotropy) given that V_{S1} is essentially isotropic (0.3 % anisotropy)(Figure 6). In particular, our V_{S1} velocity ranges from 5.55 to 5.56 km/s, while the V_{S2} ranges from 5.55 to a maximum of 6.38 km/s. Dai et al. (2013) reported an aggregate shear wave velocity of 5.601 (5) km/s, value which is very similar to that of V_{S1} obtained in this study. This suggests that in their measurements on a polycrystalline sample only V_{S1} was observed as a sharp peak, whereas V_{S2} was probably hidden in the background due to its broader appearance as a result of its large anisotropy. This is a reasonable explanation given that in the same study V_P, which has a similar anisotropy as V_{S2}, also was also not observed.

IMPLICATIONS

At pressures corresponding to ~1000 km (~40 GPa), NAL is expected to transform to the calcium ferrite type aluminum phase (CF) (Kawai and Tsuchiya 2012). According to Dai et al. (2013) such a phase transition would result in 2.5 % shear wave velocity increase. However, our zero pressure

334 shear modulus derived from single-crystal measurements is higher than the one derived from the
335 polycrystalline NAL phase by Dai et al. (2013). Single-crystal data are in general more reliable than
336 the measurements on polycrystalline samples, which can be affected by uncertainties in texture,
337 grain size, stress state, and most importantly overlook the intrinsic anisotropy of most mantle
338 minerals, such as the NAL phase. Our present result on the room pressure elasticity of the NAL
339 phase brings into question the previous conclusion of Dai et al. (2013). In fact, our zero pressure
340 elastic moduli are in good agreement with the calculations reported by Kawai and Tsuchiya (2012),
341 which argued that NAL and CF phase would have comparable shear wave velocities producing less
342 than 1% velocity difference across the phase transition. Kawai and Tsuchiya (2012) also reported a
343 significant change in the seismic wave anisotropy associated with the phase transition, which might
344 lead to a seismically detectable discontinuity as a result of favorable crystallographic preferred
345 orientation. In particular, they found that CF is significantly more anisotropic than the NAL phase.
346 Experimentally, we found that the NAL phase, displays 13.9 % compressional wave anisotropy
347 (AV_P) and shear wave anisotropy (AV_S) (Figure 6), in good agreement with the values and degree of
348 anisotropy calculated by Kawai and Tsuchiya (2012). Given the similarities in elastic constants and
349 seismic anisotropy between our study and that of Kawai and Tsuchiya (2012) at room pressure, we
350 can expect a similar behavior at higher pressures, although this still needs to be demonstrated by
351 experimentally determining the single crystal elasticity of the NAL phase and calcium ferrite phase
352 at pressures of the phase transition.
353

354 **ACKNOWLEDGEMENTS**

355 We thank S. Linhardt, H. Schulze, R. Njul, D. Krauße, U. Trentz, S. Übelhack and H. Fischer for
356 their technical assistance. We also thank R.G. Tronnes and G. Manthilake who helped during some
357 of the high-pressure experiments and F. Heidelbach for helping with anisotropy calculations.
358 Support provided by ERC advanced Grant no. 227893 ‘‘DEEP’’ funded through the EU 7th

Framework Programme. M.G.P. kindly acknowledges the support of the Bayerischen Eliteförderungsgesetz (BayEFG).

REFERENCES

Akaogi, K., Hamada, Y., Suzuki, T., Kobayashi, M., and Okada, M. (1999) High pressure transitions in the system $MgAl_2O_4$-$CaAl_2O_4$: A new hexagonal aluminous phase with implication for the lower mantle. Physics of the Earth and Planetary Interiors, 115, 67-77.

Baroni, S., de Gironcoli, S., Dal Corso, A., and Giannozzi, P. (2001) Phonons and related crystal properties from density-functional perturbation theory. Reviews in Modern Physics, 73, 515-562.

Caracas, R., and Banigan, E.J. (2009) Elasticity and Raman spectra of $MgAl_2O_4$ spinel from density functional perturbation theory. Physics of the Earth and Planetary Interiors, 172, 113-121.

Caracas, R., and Bobocioiu, E. (2011) The WURM project – a freely available web-based repository of computed physical data for minerals. American Mineralogist, 96, 437-444.

Caracas, R., and Gonze, X. (2010) Lattice dynamics and thermodynamical properties, in Thermodynamical properties of Solids: Experiment and Modelling, eds. S. L. Chaplot, R. Mittal and N. Choudhoury, WILEY-VCH Verlag, Weinheim.

Cohen, M.L. (2007). Quantum alchemy. In: Keinan, E., Schechter, I. (Eds.), Chemistry for the 21st century. Wiley-VCH.

Dai, L., Kudo, Y., Hirose, K., Murakami, M., Asahara, Y., Ozawa, H., Ohishi, Y., and Hirao, N. (2013) Sound velocities of $Na_{0.4}Mg_{0.6}Al_{1.6}O_4$ NAL and CF phases to 73 GPa determined by Brillouin scattering method. Physics and Chemistry of Minerals, 40, 195-201.

Every, A.G. (1980) General closed-form expressions for acoustic waves in elastically anisotropic solids. Physical Review B, 22, 1746-1760.

Farrugia, L.J. (1999) WinGX suite for small-molecule single-crystal crystallography. Journal of Applied Crystallography, 32, 837-838.

Gasparik, T., Tripathi, A., and Parise, J.B. (2000) Structure of a new Al-rich phase, $[K,Na]_{0.09}[Mg,Fe]_2[Mg,Fe,Al,Si]_6O_{12}$, synthesized at 24 GPa. American Mineralogist, 85, 613-618.

Gonze, X., Beuken, J.-M., Caracas, R., Detraux, F., Fuchs, M., Rignanese, G.-M., Sindic, L., Verstraete, M., Zerah, G., Jollet, F., Torrent, M., Roy, A., Mikami, M., Ghosez, Ph., Raty, J.-Y., and Allan, D.C. (2002) First-principle computation of material properties the ABINIT software project. Computational Materials Science, 25, 478-492. [http//www.abinit.org]

Gonze, X., Rignanese, G.-M., and Caracas, R. (2005) First-principles studies of the lattice dynamics of crystals, and related properties. Zeitschrift für Kristallographie, 220, 458-472.

Gonze, X., Amadon, B., Anglade, P.-M., Beuken, J.-M., Bottin, F., Boulanger, P., Bruneval, F., Caliste, D., Caracas, R., Côté, M., Deutsch, T., Genovesi, L., Ghosez, Ph., Giantomassi, M., Goedecker, S., Hamann, D.R., Hermet, P., Jollet, F., Jomard, G., Leroux, S., Mancini, M., Mazevet, S., Oliveira, M.J.T., Onida, G., Pouillon, Y., Rangel, T., Rignanese, G.-M., Sangalli, D., Shaltaf, R., Torrent, M., Verstraete, M.J., Zerah, G., and Zwanziger, J.W. (2009) ABINIT: First-principles approach to material and nanosystem properties. Computer Physics Communications, 180, 2582-2615.

Guignot, N., and Andrault, D. (2004) Equations of state of Na-K-Al host phases and implications for MORB density in the lower mantle. Physics of the Earth and Planetary Interiors, 143-144, 107-128.

Hamann, D., Wu, X., Rabe, K.M., and Vanderbilt, D. (2005). Metric tensor formulation of strain in density-functional perturbation theory. Physical Review B, 71, 035117.

Helffrich, G.R., and Wood, B.J. (2001) The Earth's mantle. Nature, 412, 501-507.

Hill, R. (1952) The elastic behaviour of a crystalline aggregate. Proceedings of the Physical Society, London, Section A, 65, 349-354.

Holzapfel, C., Rubie, D.C., Frost, D.J., and Langenhorst, F. (2005) Fe-Mg interdiffusion in $(Mg,Fe)SiO_3$ Perovskite and lower mantle reequilibration. Science, 309, 1707-1710.

Imada, S., Hirose, K., and Ohishi, Y. (2011) Stabilities of NAL and Ca-ferrite-type phases on the join $NaAlSiO_4$-$MgAl_2O_4$ at high pressure. Physics and Chemistry of Minerals, 38, 557-560.

Imada, S., Hirose, K., Komabayashi, T., Suzuki, T., and Ohishi, Y. (2012) Compression of $Na_{0.4}Mg_{0.6}Al_{1.6}Si_{0.4}O_4$ NAL and Ca-ferrite-type phases. Physics and Chemistry of Minerals, 39, 525-530.

Irifune, T., and Ringwood, A.E. (1993) Phase transformations in subducted oceanic crust and buoyancy relationships at depths of 600–800 km in the mantle. Earth and Planetary Science Letters, 117, 101-110.

Irifune, T., Koizumi, T., and Ando, J. (1996) An experimental study of the garnet-perovskite transformation in the system $MgSiO_3$-$Mg_3A1_2Si_30_{12}$. Physics of the Earth and Planetary Interiors, 96, 174-157.

Kantor, I., Prakapenka, V., Kantor, A., Dera, P., Kurnosov, A., Sinogeikin, S., Dubrovinskaia, N., and Dubrovinsky, L. (2012) BX90: A new diamond anvil cell design for X-ray diffraction and optical measurements. Review of Scientific Instruments, 83, 125102; doi: 10.1063/1.4768541

Kawai, K., and Tsuchiya, T. (2012) Phase stability and elastic properties of the NAL and CF phases in the $NaMg_2Al_5SiO_{12}$ system from first principles. American Mineralogist, 97, 305-314.

Keppler, H., and Frost, D.J. (2005) Introduction to minerals under extreme conditions. In: Miletich R. (Edt). Mineral Behaviour at Extreme Conditions. EMU Notes in Mineralogy. 7, 1-30.

Kesson, S.E., Fitz Gerald, J.D., and Shelley, J.M. (1994) Mineral chemistry and density of subducted basaltic crust at lower mantle pressures. Nature, 374, 243–245.

King, H.E., and Finger, L. (1979) Diffracted beam crystal centering and its application to high pressure crystallography. Journal of Applied Crystallography, 12, 374-378.

Kohn, W., and Sham, L.J. (1965) Self-consistent equations including exchange and correlation effects. Physical Reviews, 140, A1133–A1138.

Kojitani, H., Iwabuchi, T., Kobayashi, M., Miura, H., and Akaogi, M. (2011) Structure refinement of high-pressure hexagonal aluminous phases $K_{1.00}Mg_{2.00}Al_{4.80}Si_{1.15}O_{12}$ and $Na_{1.04}Mg_{1.88}Al_{4.64}Si_{1.32}O_{12}$. American Mineralogist, 96, 1248-1253.

Mainprice, D. (1990) An efficient Fortran program to calculate seismic anisotropy from the lattice preferred orientation of minerals. Computers & Geosciences 16, 385-393.

Martin, R.M. (2003) Electronic structure. Basic theory and practical methods. Cambridge University Press. 596 pp.

Miyajima, N., Fujino, K., Funamori, N., Kondo, T., and Yagi, T. (1999) Garnet-perovskite transformation under conditions of the Earth's lower mantle: an analytical electron microscopy study. Physics of the Earth and Planetary Interiors, 116, 117-131.

Miyajima, N., Yagi, T., Hirose, K., Kondo, T., Fujino, K., and Miura, H. (2001) Potential host phase of aluminum and potassium in the Earth's lower mantle. American Mineralogist, 86, 740-746.

Miura, H., Hamada, Y., Suzuki, T., Akaogi, M., Miyajima, N., and Fujino, K. (2000) Crystal structure of $CaMg_2Al_6O_{12}$, a new Al-rich high pressure form. American Mineralogist, 85, 1799-1803.

Monkhorst, H.J., and J.D. Pack (1976) Special points for Brillouin-zone integrations. Physical Reviews B, 13, 5188-5192.

Oxford Diffraction (2006) CrysAlis Software system, Version 171.35.19. Oxford Diffraction Ltd., Xcalibur CCD system.

Payne, M.C., Teter, M.P., Allan, D.C., Arias, T.A., and Joannopoulos, J.D. (1992) Iterative minimization techniques for ab initio total-energy calculations: molecular dynamics and conjugate gradients. Reviews of Modern Physics, 64, 1045-1097.

Sanehira, T., Irifune, T., Shinmei, T., Brunet, F., Funakoshi, K., and Nozawa, A. (2006) In-situ X-ray diffraction study of an aluminous phase in MORB under lower mantle conditions. Physics and Chemistry of Minerals, 33, 28–34.

460 Sheldrick, G.M. (2008) A short history of SHELX. Acta Crystallographica, A64, 112-122.

461 Shinmei, T., Sanehira, T., Yamazaki, D., Inoue, T., Irifune, T., Funakoshi, K., and Nozawa, A.
462 (2005) High-temperature and high-pressure equation of state for the hexagonal phase in the
463 system $NaAlSiO_4$–$MgAl_2O_4$. Physics and Chemistry of Minerals, 32, 594-602.

464 Sinogeikin, S.V., and Bass, J.D. (2000) Single-crystal elasticity of pyrope and MgO to 20 GPa by
465 Brillouin scattering in the diamond anvil cell. Physics of the Earth and Planetary Interiors. 120,
466 43-62.

467 Trots, D.M., Kurnosov, A., Vasylechko, L., Berkowski, M., Boffa Ballaran, T., and Frost, D.J.
468 (2011) Elasticity and equation of state of $Li_2B_4O_7$. Physics and Chemistry of Minerals,
469 38(7), 561-567.

470 Vanpeteghem, C.B., Ohtani, E., Litasov, K., Kondo, T., Watanuki, T., Isshiki, M., and Takemura,
471 K. (2003) The compressibility of hexagonal Al-rich NAL phase: similarities and differences
472 with calcium ferrite-type (CF) phase with implications for the lower mantle. Physics of the
473 Earth and Planetary Interiors, 138, 223-230.

474 Veithen, M., Gonze, X., and Ghosez, Ph. (2005) Non-linear optical susceptibilities, Raman
475 efficiencies and electrooptic tensors from first-principles density functional perturbation theory.
476 Physical Review B, 71, 125107.

477 Walter, M.J., Kohn, S.C., Araujo, D., Bulanova, G.P., Smith, C.B., Gaillou, E., Wang, J., Steele, A.,
478 and Shirey, S.B. (2011) Deep mantle cycling of oceanic crust: evidence from diamonds and
479 their mineral inclusions. Science, 334, 54-57.

480 Whitfield, C.H., Brody, E.M, and. Bassett, W.A (1976) Elastic moduli of NaCl by Brillouin
481 scattering at high pressure in a diamond anvil cell. Review of Scientific Instruments, 47, 942,
482 doi:10.1063/1.1134778.

483 Xu, W., Lithgow-Bertelloni, C., Stixrude, L., and Ritsema, J. (2008) The effect of bulk composition
484 and temperature on mantle seismic structure. Earth and Planetary Science Letters, 275, 70-79.

485

FIGURE CAPTIONS

FIGURE 1. Electron backscattered image showing crystals of NAL coexisting with melt. Single crystal of NAL (s5253x5) inside the diamond anvil cell at room pressure (inset).

FIGURE 2. The crystal structure of the NAL phase projected along the *c* axis. The orange octahedra correspond to the M1 sites, occupied by Al and Si. Mg, Al and Na occupy the M2 sites, represented by triangular prisms in turquoise. The ellipsoids in green elongated along the *c* axis represent Na occupying partially the M3 site.

FIGURE 3. A comparison between the experimental (solid line) and calculated (vertical grey lines) Raman spectra of the NAL phase.

FIGURE 4. Representative Brillouin spectrum of the NAL phase at a selected angle at room pressure in the diamond anvil cell.

FIGURE 5. Measured acoustic velocities for NAL sample S5253x5 (a,b,c) and S5253x3 (d,e,f) as a functions of χ angle. Solid lines are the fit of Christoffel's equation to both sets of data simultaneously. Calculated velocities from density functional theory are shown as a dashed line (this study) and dotted line (Kawai and Tsuchiya, 2012).

FIGURE 6. Single crystal compressional wave velocity (V_P), shear wave anisotropy (AV_S), fastest wave polarization (V_{S2}), V_{S2} , V_{S1} anisotropy and dV_S, plotted as Lambert azimuthal equal-area lower hemisphere pole figures (Mainprice 1990), with the elastic tensor orthogonal axes X1 = *a* axis (east) and X3 = *c* axis (centre).

Table 1. Structural refinement details

and unit cell parameters of the NAL phase

Measured reflections	1623
Unique reflections	328
Fo > 4sig(Fo)	308
Rint	3.05%
Rw for Fo > 4sig(Fo)	2.85%
Rall	3.19%
wR2	7.12%
GooF	1.109
No. parameters	24
Space group	$P6_3/m$
Z	1
Crystal size	70x50x15 μm^3
F(000)	235
Absorption coefficient	1.49 mm^{-1}
Unit-cell parameters	
a(Å)	8.7225(4)
c(Å)	2.7664(2)
V(Å^3)	182.3(2)

517

518

519

520

Table 2. Experimental atomic coordinates and displacement parameters of the NAL phase

Site	Wyckoff position	x	y	z	U_{11}	U_{22}	U_{33}	U_{12}	U_{eq}
M1	6*h*	0.98946(8)	0.34353(9)	1/4	0.0058(3)	0.0057(3)	0.0053(3)	0.0029(2)	0.0056(2)
M2	2*d*	2/3	1/3	1/4	0.0093(4)	0.0093(4)	0.0094(6)	0.0047(2)	0.0093(3)
M3	2*a*	0	0	1/4	0.007(1)	0.007(1)	0.25(2)	0.0035(5)	0.089(7)
O1	6*h*	0.1283(2)	0.5989(2)	1/4	0.0069(6)	0.0070(6)	0.0125(7)	0.0029(5)	0.0090(3)
O2	6*h*	0.3124(2)	0.2024(2)	1/4	0.0090(7)	0.0088(6)	0.0100(7)	0.0053(5)	0.0089(3)

521

522

Table 3. Comparison of the interatomic distances and angles between two NAL phases.

	NAL this study	NAL Kojitani et al. (2011)
Sites	**Distance (Å)**	
M1-O2 x2	1.838(1)	1.817(3)
M1-O2'	1.881(2)	1.890(4)
M1-O1'	1.932(2)	1.903(5)
M1-O1 x2	1.933(1)	1.940(3)
M2-O1 x6	2.098(1)	2.128(3)
M3-O2' x3	2.394(2)	2.393(3)
M3-O2 x6	2.765(1)	2.764(3)
O2-O2'	2.765(3)	2.764(3)
O1-O1'	2.457(2)	2.373(6)
	Bond angle (°)	
O2-M1-O2	97.61(8)	99.2(2)
O2'-M1-O2 x2	96.02(8)	96.45*
O2 x2-M1-O1'	95.46(6)	95.74*
O2'-M1-O1'	162.53(8)	161.2(2)
O2-M1-O1 x2	173.99(7)	171.55*
O2-M1-O1 x2	85.27(5)	84.48*
O2'-M1-O1 x2	88.89(6)	90.7(2)
O1'-M1-O1 x2	78.98(7)	76.3(2)
O1-M1-O1	91.38(7)	90.9(2)
O1-M2-O1 x3	82.48(6)	81.07*
O1-M2-O1'' x6	135.83(2)	135.33*
O1'-M2-O1'' x6	81.27(4)	82.32*

*Calculated value using the data from Kojitani et al. (2011)

523

524

525

Table 4. Experimental and calculated Raman modes of the NAL phase at room pressure.

ν obs (cm^{-1})	ν calc (cm^{-1})	I calc* (symmetry label)	Description
	148.35	0.31 (E")	Na atoms vibrating in plane
	199.54	0.05 (E")	Lattice mode; stretching of the octahedral framework of channels
	218.62	0.03 (A')	Lattice mode; Tilt of the channel walls
	223.13	0.17 (E')	Lattice mode; Mainly Si movements (octahedral sites) along the z axis
	238.22	0.03 (E")	Lattice mode; Tilts of the channels; rigid motion of the polyhedral sub-lattice
	266.54	0.15 (A')	Lattice mode; Tilts of the channels; rigid motion of the polyhedral sub-lattice
272.5	268.83	0.56 (E")	Stretching of the Si-O-Al angle
	317.35	0.29 (A')	Tilts of the octahedra from the channels' walls
370.6	351.99	1.00 (A')	Has a strong breathing component of the SiO_6 octahedra
	400.04	0.18 (E")	Breathing of the Si-Al-Si cavities
	433.14	0.01 (A')	Tilt of the Al polyhedra;
	458.34	0.27 (E')	Tilt of the Al polyhedra
487.63	465.58	0.35 (E')	O-Si-O rigid tilt of the octahedra
507.97	472.55	0.12 (E")	Asymmetric stretching of the Al-O polyhedra
553.16	514.59	0.24 (A')	Asymmetric stretching of the Si-O bonds of the octahedral
	515.15	0.08 (E')	Rolling mode of the apical Si-O bonds in the octahedra
	529.74	0.17 (E')	Rolling mode of the apical Si-O bonds in the octahedra
	557.51	0.03 (E")	Si-O stretching mode in the octahedra
	663.07	0.08 (E")	O-Si-O stretching mode
735.73	691.32	0.92 (A')	Breathing mode of the Al-O polyhedra
757.65	706.43	0.04 (A')	Breathing mode of the Si-O octahedra
	713.84	0.05 (A')	Asymmetric stretching of the Si-O bonds of the octahedral
	757.43	0.01 (E")	Asymmetric stretching of the Al-O polyhedra
	780	0.02 (E")	Breathing mode of the Si-O octahedra
1091.38	-	-	Overtone of the 553 cm^{-1} band or combination mode

* relative intensities

526

527

528

Table 5. Elastic constants and aggregate properties of the NAL phase at room pressure.

	$Na_{1.07}Mg_{1.58}Al_{4.91}Si_{1.26}O_{12}$ experimental (this study)*	$Na_{1.3}Mg_{1.6}Al_{4.9}Si_{1.2}O_{12}$ theoretical (this study)	$NaMg_2Al_5SiO_{12}$ theoretical [a]	$Na_{0.4}Mg_{0.6}Al_{1.6}Si_{0.4}O_4$ experimental [b]
C_{11}	365	326	390	-
C_{12}	126	99	137	-
C_{13}	100	77	98	-
C_{33}	477	457	510	-
C_{44}	119	116	128	-
K_s	206	178	217	-
μ	129	125	138	121.96 (9)
V_p	9.9	9.99	10.1	9.643 (9)
V_s	5.8	6.01	5.90	5.601 (5)
ρ	3.86	3.45	3.97	3.89 [c]

[a] Kawai and Tsuchiya (2012), [b] Dai et al. (2013), [c] density from data reported by Imada et al. (2012).* In this study uncertainties in elastic moduli and in sound velocities are less than 2 % and 1 %, respectively.

529

530

531

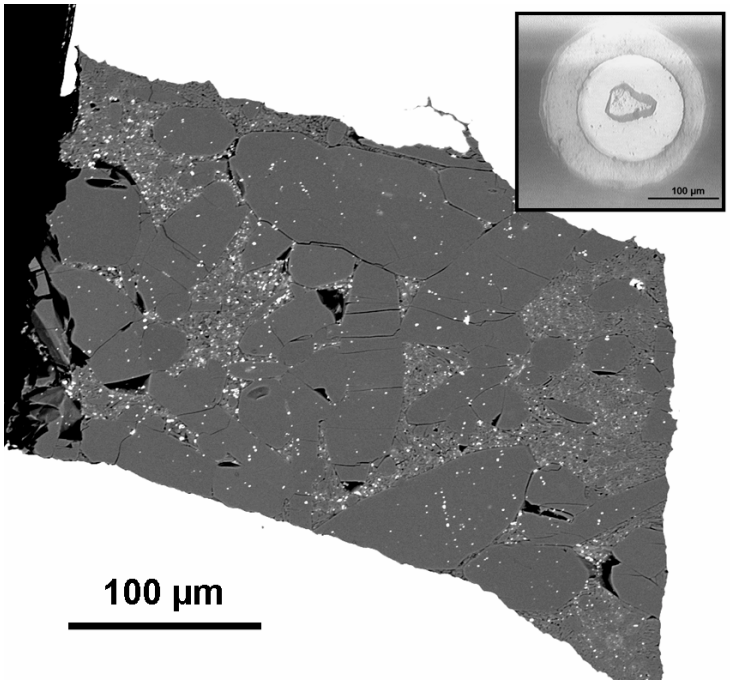

532

533 Figure 1.

534

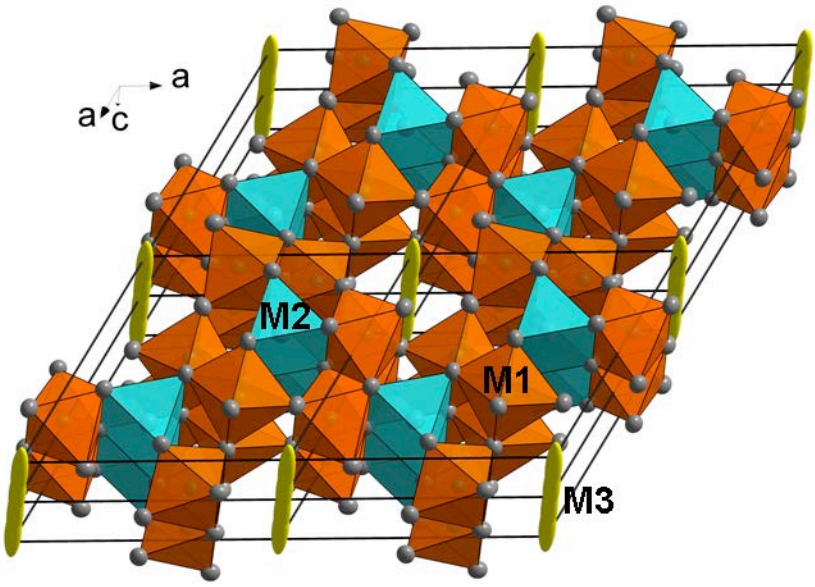

535

536 Figure 2.

537

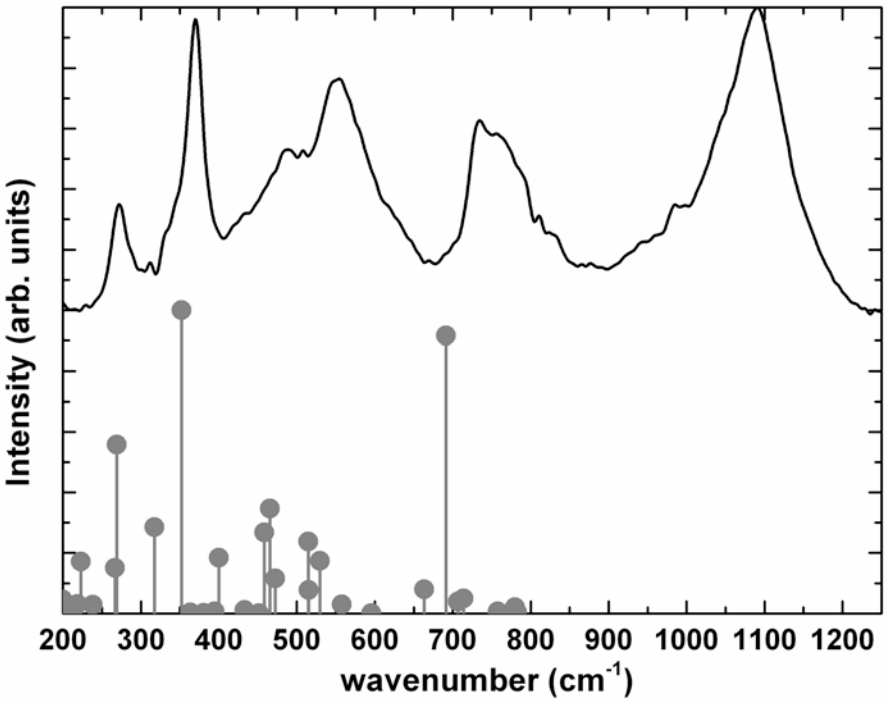

538

539 Figure 3.

540

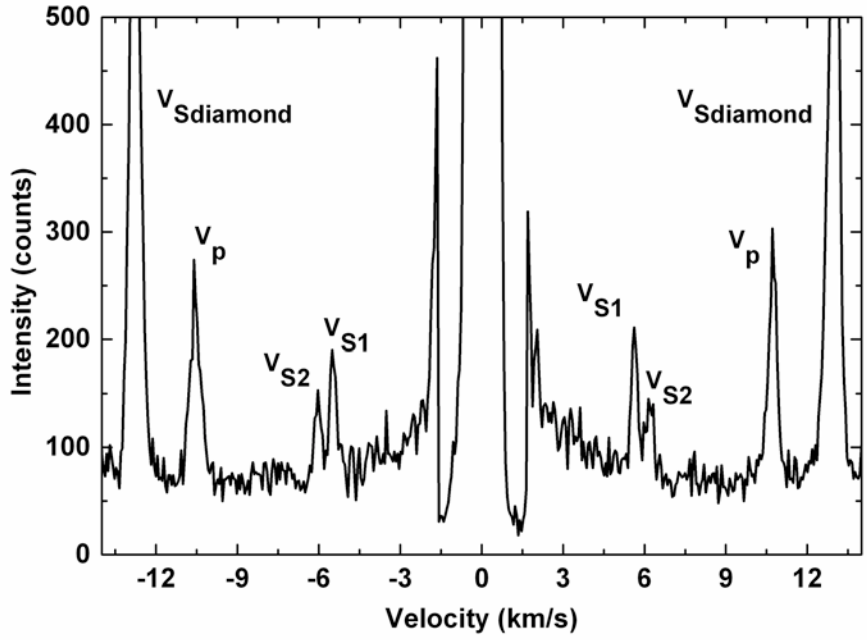

541

542 Figure 4.

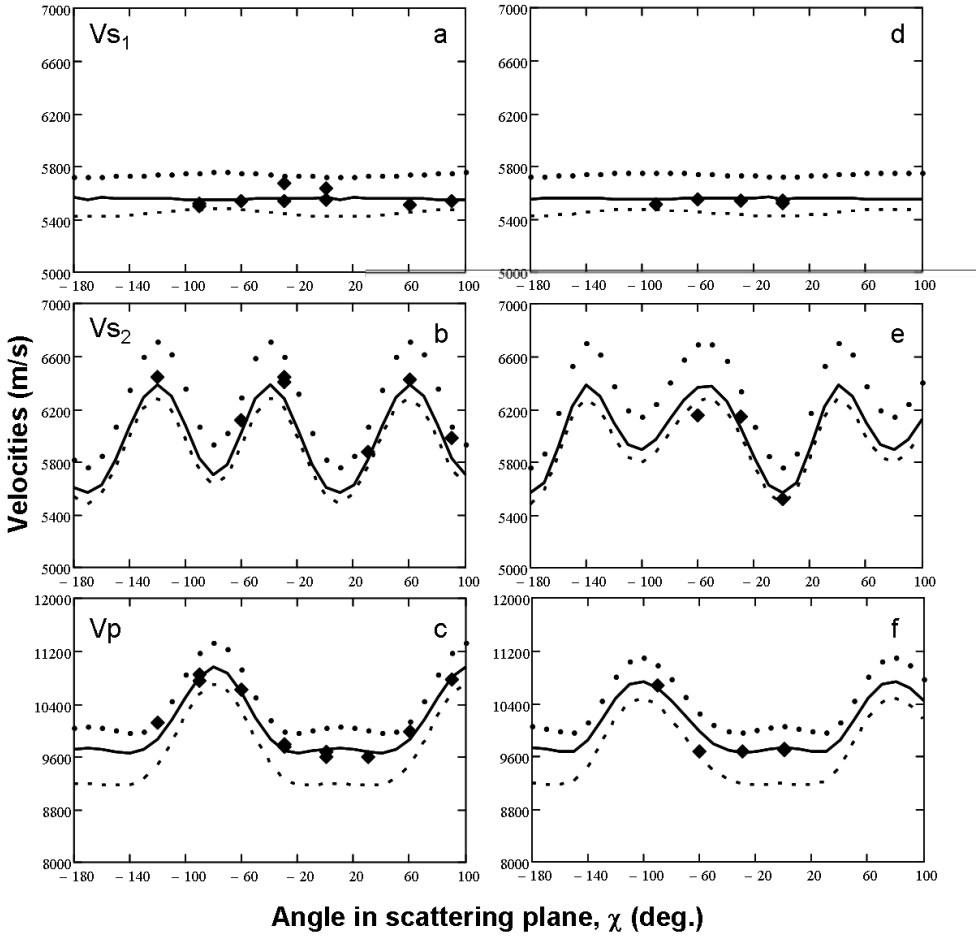

Figure 5.

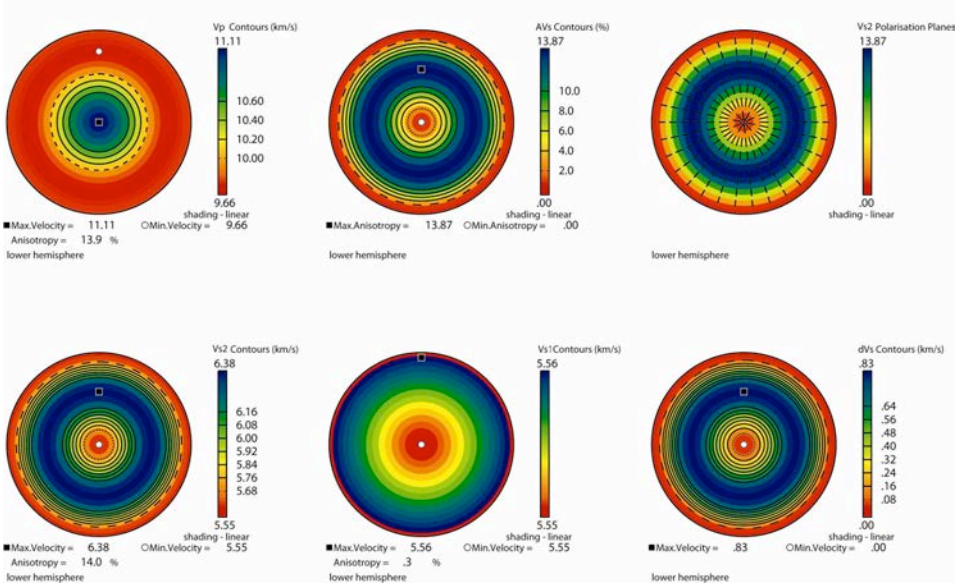

Figure 6.